Ocean Sci. Discuss., 4, 145–187, 2007
www.ocean-sci-discuss.net/4/145/2007/

Ocean Science Discussions

Papers published in *Ocean Science Discussions* are under open-access review for the journal *Ocean Science*

"Scale oriented" embedded modeling of the North-Western Mediterranean in the frame of MFSTEP

C. Estournel[1], F. Auclair[1], M. Lux[2], C. Nguyen[1], and P. Marsaleix[1]

[1]Pôle d'Océanographie Côtière de Toulouse – Laboratoire d'Aérologie, Toulouse, France
[2]Noveltis, Toulouse, France

Received: 30 October 2006 – Accepted: 26 January 2007 – Published: 12 February 2007

Correspondence to: C. Estournel (claude.estournel@aero.obs-mip.fr)

Abstract

An embedded forecasting system was developed for the North-Western Mediterranean including a regional model and a coastal model of the Gulf of Lion. The system is based on the Symphonie hydrodynamic free surface model and on the variational initialization and forcing platform VIFOP. It was shown that a pre-modeling period of 7 days before beginning the forecast allows the growth of the small scales. The embedded forecasts have been compared to the MFS observing system. It was basically found that in the North-Western Mediterranean, the MFS basin-scale model and thus the regional model forecasts are characterized by large negative biases of salinity in the first 100m under the surface leading thus to too light subsurface waters. The underestimation of temperature by the regional model just below the surface and its overestimation at 30 m deep can be associated to an overestimation of the turbulent mixing. The regional and coastal models allow to represent a number of processes especially those induced by the wind as coastal upwelling under stratified conditions, dense water formation over the Gulf of Lion shelf, deep mixing in the convection zone or influence on the Northern Current penetration in the Gulf of Lion.

1 Introduction

The regional modeling of the North-Western Mediterranean (NWM) is carried out in the frame of the Mediterranean Forecasting System (MFS). The MFS offered indeed a unique opportunity for both coastal and regional ocean modelers to jump from their classical "process oriented" studies to further "scale oriented" studies. First of all, the second part of the MFS (Toward Environmental Predictions or MFSTEP) has been a successful observation laboratory of the Mediterranean over a large variety of physical scales. It also comes in the continuity and consolidates the objectives of the MFS Pilot Project (MFSPP) during which a clear embedded strategy had been proposed (Pinardi et al., 2003) and basin scale modeling had been carried out successfully (Demirov and

OSD

4, 145–187, 2007

Pinardi, 2002). To end up with, the coupling of physical and biochemical models has been proposed with a common forecasting objective.

To be successfully achieved, the regional modeling of the NWM has eventually been based not only on an observing system, but also on quality meteorological forecasts and analysis and on basin scale modeling. As dynamically opened systems, both coastal and regional ocean modeling are indeed completely dependent on the quality of the various forcing. We thus clearly defend the idea that no small scale modeling strategy can be achieved without a strategy based on quality checks at every scale. As a consequence, we think that the regional or coastal modeler, far from being a modeler on its own, must be part of a cooperating team. At the opposite, basin scale modelers cannot pretend studying large scale circulation without some precise quality checks along the shelf breaks and the coasts. The MFS has grounded such believes in its basic strategy and is thus a source of scientific achievements.

The MFSTEP consequently includes more particularly two essential scientific grounds without which no coastal or regional modeling can be achieved: the ocean forecasting is first seen as a "scale oriented problem" and observing and numerical modeling strategies are designed as complementary components.

Several scientific objectives were more specifically achieved during this project and are detailed in the present paper. First of all, by carrying out realistic long term regional modeling, the NWM dynamical processes could be studied in details and validated based on several types of observations. As stated above, the MFS is also a unique opportunity to test and validate in an operational context the embedded modeling strategy proposed and developed at the POC in terms of open boundary conditions (Marsaleix et al., 2006) and initialization (Auclair et al., 2006). The regular distribution of forecasted fields[1] through the web in this "best effort context" implies both technical and scientific constrains. Scientifically first, this means that embedded models can in-

[1] A weekly forecasting bulletin is provided by NOVELTIS for the north-western Mediterranean region and for the Gulf of Lion coastal zone. These bulletins are available at http://www.noveltis.fr/mfstep-wp9

clude no spin up period as even one-day forecast must be dynamically accurate. The embedded strategy has thus to be revisited and validated based on more demanding requirements. Technically, this means that the operational delivery has to be based on a computationally affordable and stringent numerical treatment. The treatment must also offer several levels of regional and coastal forecasting depending on the availability of the forcing fields while the strongest level of automatic and human checking insures an optimal coherence of the dynamical fields.

In the following, the proposed regional modeling strategy is presented in details in Sect. 2. Then the regional forecast is compared to dedicated observations (Sect. 3) and several physical processes are studied at well identified spatial scales (Sect. 4).

2 The NWM regional modeling system

2.1 Previous applications of hydrodynamic modeling in the North Western Mediterranean Sea

The MFS numerical strategy was not restricted to a single type of regional models as the POM and SYMPHONIE models have been implemented in specific regions. As far as the NWM is concerned, the modelling strategy was based not only on the SYMPHONIE model but also on the experience accumulated over years by the POC in this area. This experience covers indeed the modelling of the NWM oceanic circulation at regional scale, several studies of the coastal dynamics of the shelf of the Gulf of Lion, and eventually, at smaller scales, near-shore studies based on high resolution implementations of the hydrodynamic model.

At the regional scales, the oceanic circulation is principally characterized by the Liguro-Provençal-Catalan (LPC) current (or Northern Current). This current is highly constrained by the shelf break slope. As the continental shelf is rather narrow in the NWM Sea, the Northern current tends to stick to the coast, except in the Gulf of Lion where the continental shelf is much larger. In this latter case, the Northern current

flows mainly above the shelf break slope, about 100 km offshore in the region of the Gulf of Lion, but secondary currents can flow onto the continental shelf, as shown by Petrenko et al. (2005). Auclair et al. (2001) studied this process from a numerical point of view. As far as short time scales are concerned (a critical issue since the MFSTEP regional forecasts do not extend over one week), they showed that the unbalance of the initial state, resulting from inconsistencies between the interpolated Mediterranean basin model solutions and the local complex bathymetry, could be disastrous for the dynamics of current intrusions onto the continental shelf.

At the scale of the continental shelf of the Gulf of Lion, the oceanic circulation is dominated by local winds. Because of the particular orography of the South of France, these winds are channelled. Estournel et al. (2003) showed that the wind stress curl, associated to Tramontane and Mistral, could explain the meso-scale eddy circulations developing over the whole shelf. The possible suddenness and strength of these winds are likely to cause strong inertial oscillations of the current (Petrenko et al., 2005) and coastal upwelling, preferentially developing along rectilinear sections of the coast (Johns et al., 1992). In winter, these winds, rather dry and cold, extract a large amount of heat from the water column. As exposed areas react all the more that the water column is shallow, temperature in near shore areas eventually strongly decreases. Dufau-Julliand et al. (2004) showed that the dense water lenses, formed through that process on the Gulf of Lion shelf, sink along the bottom slope and that the western canyons were the principal pathway between the continental shelf and the deep sea area. The formation of dense waters over the shelf is nevertheless limited by buoyancy effects as fresh waters are brought by local rivers. Because of its strong freshwater discharge (actually the largest river discharge of the whole Mediterranean Sea), the Rhone river is an important source of potential energy that significantly influences the shelf circulation of the Gulf of Lion. Because of the atidal context, the Rhone plume is slowly diluted with oceanic waters. The surface lenses, formed in the river mouth area, are only a few meter thick and their response to local wind variations is rather quick. Estournel et al. (1997, 2001), Marsaleix et al. (1998) and Reffray et al. (2004) studied

the dynamic of the Rhone river plume, showing that the Symphonie physical model could reproduce the sharp vertical stratification as well as the quick displacements of frontal horizontal patterns.

At small scales and close to the coast, Ulses et al. (2005) and Guizien et al. (2006) showed that the model could reproduce the principal characteristics of the circulation, more particularly in the bay of Banyuls and in the Gulf of Fos. Thanks to the numerous in situ and satellite observations, all the previously mentioned studies have brought different kinds of validations.

2.2 Description of the model

A short description of the SYMPHONIE physical model is now given. The reader can refer to the previously mentioned papers for complementary information.

The components of the current, the temperature and the salinity are computed on a staggered C-grid thanks to a classic finite difference method. The model is "free surface", in such a way that high frequencies barotropic processes are explicitly represented. Solving surface waves is known to potentially increase computing costs. We limit this drawback by computing the baroclinic and barotropic velocity components separately, based on well adapted separated time steps, according to the time-splitting method proposed by Blumberg and Blumberg and Mellor (1987). Vertical turbulent fluxes are parameterised thanks to the turbulence closure scheme, based on one prognostic equation for the turbulence kinetic energy and on two length scales (for mixing and dissipation) proposed by Gaspar et al. (1990). Small scale horizontal processes, unresolved by model equations because of limitations due to the grid length scale, are parameterized through a Laplacian-type mixing operator. The horizontal mixing coefficient remains constant, as far as currents are concerned. Practically, the latter is equal to $15\,m^2\,s^{-1}$ in the case of the regional model and to $7.5\,m^2\,s^{-1}$ in the coastal implementation. An adaptative horizontal diffusivity is used for tracer equations in order to limit the overshoot effects of the first order centered advection scheme.

As in most coastal models, a sigma coordinate system provides a realistic repre-

sentation of the bathymetry. As far as the NWM is concerned, this is a critical issue insofar as the Northern current is largely guided by the continental slope. The sigma-coordinate also enables to maintain a fine vertical resolution near the bottom, a significant asset since the bottom turbulence layer is likely to play a major role in the equilibrium of continental shelf circulations (Dufau-Julliand et al., 2004).

On the other hand, the sigma coordinate is known to present some serious shortcomings. Among them, the accuracy of the pressure gradient is probably the most well known. Another shortcoming concerns the possible lack of vertical resolution in deep sea areas, or alternatively, an excessive number of vertical levels in shallow areas consequently leading to a drastic reduction of the time step in order to ensure numerical stability. Many authors have proposed compromises to reduce those drawbacks: Adcroft et al. (1997) used for instance a Cartesian system combined to a bottom-following first level (the so-called partial step coordinate), and Auclair et al. (2000a) proposed a two-fold sigma coordinate in order to keep the upper levels close to the Cartesian system. Another compromise is to use a generalised topography following coordinate system (Pietrzak et al., 2002). Such coordinates provide some degrees of freedom in the definition of the position of vertical levels, providing for instance a way to optimize the vertical distribution within surface or bottom layers. However, this system does not allow to efficiently control the slope of the deeper levels and to eventually avoid, for some of them, the situation of hydrostatic inconsistency (Haney, 1991), unfavourable to pressure gradient computation. We propose here to combine a generalized topography following coordinate system with a "staircases" system. This "hybrid" coordinate system consists in skipping over a vertical level, as the classic Cartesian system does, when the bathymetry is too steep for the sigma level to follow the bottom slope without creating a situation of hydrostatic inconsistency. Another advantage of the so-called "step coordinate system" is also to limit the number of vertical levels in very shallow areas, as for instance in the Rhone river mouth area, where the bottom depth reaches approximately 2 m. In our model, the Rhone estuary is partly modelled through a waterway, a few grid points long. Currents are locally very strong and a classic sigma

coordinate system, including the complete set of vertical levels (40 levels in the present case), would severely restrict the time step for CFL stability reasons, among which appears the need for advection schemes to deal with current numbers lower than 1. Our hybrid "sigma-step" allows the use of only 5 levels in the Rhone river waterway. The principal equations of the model, formulated within the sigma coordinate system, are presented in Appendix A.

2.3 Open boundary conditions

River runoff:

The specification of the river run-off forcing is a key step of any modeling effort of the NWM. Indeed, this region includes the Rhone river mouth, which, with a 1700 m^3/s annual mean discharge is the largest in the Mediterranean basin. It has in particular a crucial impact on the dynamics of the Gulf of Lion. As shown in Estournel et al. (2001), the boundary condition is specified at the river mouth for the normal component of the horizontal velocity, and for both temperature and salinity at the upstream neighboring point. A vanishing salinity is imposed while a climatological annual variation is specified for temperature. A logarithmic profile is imposed for the current associated to a mass conservation criterion to insure that the river runoff is correctly specified:

$$L \int_{-h}^{\eta} u dz = F$$

where L is the river mouth width (in the NWM, the river boundary condition is specified over only one grid point, so that L=Δx) and F is the observed river discharge in $m^3\,s^{-1}$. In hindcast mode, the daily discharges for both the Rhone and Ebro Rivers are taken from CNR[2] and SAIH Ebro[3]. In the Gulf of Lion coastal model, smaller rivers are

[2]CNR : http://www.cnr.tm.fr

[3]SAIH Ebro : http://195.55.247.237/saihebro/

taken into account on the basis of climatological discharges. In forecast mode, river discharges remains constant and are taken equal to the last available observation.

Surface conditions:

Surface boundary conditions for diffusion terms in temperature, salinity, and horizontal momentum equations (Appendix A) are respectively given by heat (Q), salt (S) and momentum (τ) surface fluxes following:

$$K_v \frac{\partial T}{\partial z} = Q\left(\rho C_p\right)^{-1}, \quad K_v \frac{\partial S}{\partial z} = F\rho^{-1}S, \quad K_v\left(\frac{\partial u}{\partial z}, \frac{\partial u}{\partial z}\right) = (\tau_u, \tau_v)\,\rho^{-1} \tag{1}$$

where C_P is the ocean heat capacity (3950 J/kg/K). The heat flux includes short wave (or solar) radiation (Q_S), long wave radiation (Q_L), (turbulent) sensible (Q_H) and latent (Q_E) heat fluxes. The salt flux is made of precipitation (P) and evaporation (E) fluxes. This latest component is directly related to the latent heat flux ($Q_E \approx 2.5\times10^6 E$).

The turbulent heat fluxes are estimated through bulk formulae (Geernaert 1990):

$$\begin{aligned} E &= \rho_a C_E (q_{2\,\mathrm{m}} - q^{\mathrm{sat}}_{0\,\mathrm{m}})\,|\boldsymbol{U}_{10\,\mathrm{m}}| \\ Q_H &= \rho_a C_H (\theta_{2\,\mathrm{m}} - T_{0\,\mathrm{m}})\,|\boldsymbol{U}_{10\,\mathrm{m}}| \\ \boldsymbol{\tau} &= \rho_a C_D\,|\boldsymbol{U}_{10\,\mathrm{m}}|\,\boldsymbol{U}_{10\,\mathrm{m}} \end{aligned} \tag{2}$$

where $\boldsymbol{U}_{10\,\mathrm{m}}$ is the 10 m high wind, $q_{2\,\mathrm{m}}$ and $\theta_{2\,\mathrm{m}}$ are respectively the air specific humidity and the potential temperature in Kelvin at 2 m high above sea surface, $\rho_a \approx 1.226\,\mathrm{kg\,m^{-3}}$ is the reference air density and $T_{0\,\mathrm{m}}$ the sea surface temperature in Celsius. The air at the surface is assumed to be saturated, with a specific humidity deduced from saturated vapor pressure (p_{vs}), saturation mixing ratio (r) and surface atmospheric pressure ($p_{0\,\mathrm{m}}$):

$$\begin{aligned} q^{\mathrm{sat}}_{0\,\mathrm{m}} &= 0.98 r/(1+r)) \\ r &= 0.622 p_{vs}/(p_{0\,\mathrm{m}} - p_{vs}) \end{aligned}$$

$$p_{vs} = 610.78\, e^{\frac{17.27 T_{0\,\mathrm{m}}}{T_{0\,\mathrm{m}}+237.29}} \tag{3}$$

OSD
4, 145–187, 2007

The drag coefficient (C_D) and the transfer coefficient for evaporation (C_E) and sensible heat (C_H) are functions of atmospheric stability (ς) and wind speed. Their neutral stability values, used to start the iterative procedure, are given by:

$$\begin{aligned} C_{DN} &= \max\left(0.93\times10^{-3},\ 0.61\times10^{-3}+6.3\times10^{-5}\,|\boldsymbol{U}_{10\,\mathrm{m}}|\right)\\ C_{EN} &= 1.2\times10^{-3}\\ C_{HN} &= 0.7\times10^{-3} \quad \text{stable} \quad \varsigma>0\\ C_{HN} &= 1.2\times10^{-3} \quad \text{unstable} \quad \varsigma\le 0 \end{aligned} \tag{4}$$

with

$$\varsigma(z)=\frac{g\,k\,z}{u*^2}\,\frac{t*\,(1.+0.608\,q_{10\,\mathrm{m}})+q*0.608\,\theta_{10\,\mathrm{m}}}{\theta_{10\,\mathrm{m}}\,(1.+0.608\,q_{10\,\mathrm{m}})} \tag{5}$$

where k=0.4 is the von Karman constant, and $u*$, $t*$, $q*$, the turbulent scales given by:

$$\begin{aligned} u* &= \sqrt{C_D}U_{10\,\mathrm{m}}\\ t* &= C_H U_{10\,\mathrm{m}}\,\frac{\theta_{10\,\mathrm{m}}-(T_{0\,\mathrm{m}}+273.15)\left(\frac{10^5}{p_{0\,\mathrm{m}}}\right)^{0.286}}{u*}\\ q* &= C_E U_{10\,\mathrm{m}}\,\frac{q_{10\,\mathrm{m}}-q^{\mathrm{sat}}_{0\,\mathrm{m}}}{u*} \end{aligned} \tag{6}$$

In this expression, the 10 m height values have been deduced from the 2 m ones according to:

$$\begin{aligned} q_{10\mathrm{m}} &= q_{2\,\mathrm{m}}+\frac{q*}{k}\left(\ln\left(\frac{10}{2}\right)-\varphi\left(\zeta_{10\,\mathrm{m}}\right)+\varphi\left(\zeta_{2\,\mathrm{m}}\right)\right)\\ \theta_{10\,\mathrm{m}} &= \theta_{2\,\mathrm{m}}+\frac{t*}{k}\left(\ln\left(\frac{10}{2}\right)-\varphi\left(\zeta_{10\,\mathrm{m}}\right)+\varphi\left(\zeta_{2\,\mathrm{m}}\right)\right) \end{aligned} \tag{7}$$

The functions $\varphi_m(\zeta)$ and $\varphi_h(\zeta)$ are given by:

$$\begin{aligned}
&\varphi_m(\zeta) = \varphi_h(\zeta) = -7\,\zeta \quad \text{stable}, \quad \zeta \geq 0 \\
&\varphi_m(\zeta) = 2\ln\left(\tfrac{1+X}{2}\right) + \ln\left(\tfrac{1+X^2}{2}\right) - 2\tan^{-1}(X) + \tfrac{\pi}{2} \quad \text{unstable}, \quad \zeta < 0 \\
&\varphi_h(\zeta) = 2\ln\left(\tfrac{1+X^2}{2}\right) \quad \text{unstable}, \quad \zeta < 0 \\
&X = (1 - 16\zeta)^{1/4}
\end{aligned} \tag{8}$$

and C_D, C_E, C_H are eventually given by:

$$\begin{aligned}
C_D &= C_{DN}\left(1 - \frac{\sqrt{C_{DN}}}{k\varphi_m(\zeta_{10\,\mathrm{m}})^2}\right) \\
C_H &= C_{HN}\sqrt{\frac{C_D}{C_{DN}}}\left(1 - \frac{C_{HN}}{k\sqrt{C_{DN}}\varphi_h(\zeta_{10\,\mathrm{m}})}\right) \\
C_E &= C_{EN}\sqrt{\frac{C_D}{C_{DN}}}\left(1 - \frac{C_{EN}}{k\sqrt{C_{DN}}\varphi_h(\zeta_{10\,\mathrm{m}})}\right)
\end{aligned} \tag{9}$$

Practically, hourly values of the wind at 10 m high, of the surface pressure, of the specific humidity, of the air temperature at 2 m high, of the precipitation, of the solar radiation and of the longwave radiation received by the ocean from the atmosphere (Q_A) are provided by the meteorological model ALADIN (Brozkova et al., 2006). The net longwave flux is deduced from Q_A thanks to the sea surface temperature and the Stefan constant (σ=5.67 × 10^{-8} W m^{-2} K^{-4}):

$$Q_L = Q_A - \sigma T_{0\,\mathrm{m}}^4 \tag{10}$$

Lateral open boundary conditions:

Open boundary conditions (OBC) are discussed in details in Marsaleix et al. (2006) and are thus briefly presented here. Classically, OBC endorse here a double purpose: they are first of all required to force the inner solution with the external fields obtained from the large-extent model (the basin model forces the regional, the latter forces the coastal

model) and at the same time, they must allow waves to radiate out or water masses to leave the modelling domain under outgoing conditions, without any spurious reflections. The Flather scheme gives a boundary condition for the sea surface elevation. A zero gradient condition is applied to the tangential component of the transport while its normal component is deduced from the two former variables combined to the inversion of the barotropic continuity equation. Marsaleix et al. (2006) showed that such an implementation of the Flather conditions offers interesting properties of mass and energy conservation. A wave-equation-type condition, or Sommerfeld condition, based on a constant wave speed of 1 m/s, is applied to the baroclinic horizontal velocities. The tracer condition is simply given by the inner advection diffusion equation (Appendix A, equations A4 and A5) but with an upstream version of the advection scheme in order to make the external water masses enter the numerical domain under inflow conditions. OBC are combined with a restoring condition toward the external field within a nudging layer, in the vicinity of open boundaries. Within this layer a restoring term is added to the momentum and tracer equations. This term, which is progressively vanishing with the distance to the open boundary (practically the layer is 15 grid points wide), is inversely proportional to a time scale equal to one day (for baroclinic velocities and tracer equations) and to 0.05 day (for barotropic velocities equations) at the closest grid nodes to the boundary.

2.4 Operational forecasting system for embedded modeling

Two implementations are proposed at two different scales: one is a regional modeling of the NWM based on a 3 km×3 km grid while the other is a coastal modeling of the Gulf of Lion based on a 1.5 km×1.5 km grid (Fig. 1). The hybrid vertical sigma grid has a maximum of 40 levels above the abyssal region, 20 levels over the shelf and only 5 levels in the shallower regions, such the Rhone river mouth. A rotation of the model grid with respect to the North-South direction is made in order to optimize the modeling of the cyclonic regional circulation made of the Northern Current along the Northern coastline (Millot, 1990).

At forecasting scales, i.e. a few days, the model "spin up" remains a challenging problem. Indeed, "spin up" has classically been considered as a troublesome but "self resolving" difficulty. If long, tedious spin up periods could be carried out in process oriented studies, it cannot be tolerated in realistic "scale oriented" modelling whether operational or not (Auclair et al., 2006).

Over the shelf break and in the coastal region, the bathymetry mismatches between the low and high resolution models necessarily break the fundamental physical balances (Auclair et al., 2000b or Auclair et al., 2006). A two step strategy is thus proposed for the NWM embedded modeling.

VIFOP optimization:

Optimal extrapolation and mass balance enforcement are carried out before larger scale fields are used to initialize and force the embedded, high resolution model along its open boundaries. This is obtained thanks to the Variational Initialization and Forcing Platform (VIFOP). The objective of this variational optimization strategy is first to ensure that the forcing fields satisfy the fundamental masse balance. As a consequence, no spurious mass exchange can appear associated for instance to a crude interpolation scheme over regions showing large bathymetry mismatches. The second objective is to drastically reduce the generation of surface gravity waves due to a local mass unbalance. Such waves have been shown to last for a few hours to several days following the initialization (Auclair et al., 2000b). The optimal extrapolation is used to initialize regions where no information is available (Auclair et al., 2006). Such regions can in particular be found along the shelf break where the General Circulation Model (GCM) bathymetry can be several tenths of meters shallower than the high resolution embedded model. In these areas, crude interpolation most often lead to the generation of spurious geostrophic currents which can hardly be separated from physically coherent along shelf currents (Auclair et al., 2006).

Small scale spin-up:

On the other hand, small scale turbulence together with small scale ocean dynamics associated for instance to atmospheric forcing cannot be a priori adjusted at the initial time step and usually take a few days to build up and adjust. Indeed, regional models are basically used to downscale the GCM large scale dynamics in which XBT and satellite observations have both been assimilated. They are thus based on a high quality large scale dynamics and, thanks to their higher resolution, they additionally provide smaller scale dynamics. In the frame of the MFS, five-day forecasts are issued and small scale dynamics must have grown up to their realistic level at the beginning of the forecast. The regional modeling must thus begin a few days before the forecast period.

The pre-modelling/forecast strategy:

If a few-day "pre-modeling" has thus to be systematically carried out before the forecast period, this period must remain as short as possible for at least two reasons. In one hand, coastal ocean previsibility is not infinite and on the other hand, the CPU time must remain affordable. As a compromise, a one-week period is chosen for pre-modeling. During the very first week, the embedded model is forced at its free surface by analyzed atmospheric fluxes, along its open boundaries by GCM analysis and, when available, in-situ observations are used for river discharges. Then, the same numerical run is pursued during 5 days in forecasting mode, based on atmospheric and oceanic forecasts. This procedure is repeated every week.

In order to clearly evaluate the quality of such forecasts during the 6-month "TOP" of the MFSTEP, a similar regional modeling is conducted in which only analyses are used for atmospheric, oceanic and river forcing. This "hindcast" modeling is used as a reference to evaluate the quality of the forecasts.

3 Evaluation of the forecasting system

3.1 Diagnostics on embedded forecast

A set of six forecast periods has been selected and is now analyzed in details. Three of them are chosen at the end of the summer period (September–October), i.e. for stratified conditions in the upper ocean, while the remaining three forecast periods are chosen in winter, i.e. for well mixed conditions.

Pre-modelling period:

Figure 2 shows the time evolution of the current intensity averaged over the 6 selected forecast periods and over the domain. In order to clearly extract the spin up of the small scale structures, the current has been decomposed as $V=\bar{V}+V'$ where $\bar{V}$ is the large scale component and V' is the small scale anomaly. The large scale component of the current is computed as the windowed averaged current over a 33 km square box around each grid point. To be compared, both regional and GCM fields have been averaged over a 24-h period.

We can globally notice that the obtained large scale currents are rather similar and show in particular the same temporal variations. The regional model large scale current is yet slightly larger than the GCM large scale current.

At smaller scales, the GCM currents are, as could be expected, rather small while the regional model, thanks to its higher resolution, progressively grows a small scale dynamics starting at the initialization date. It can be noticed that the growth of these smaller scales is rather steep during the pre-modeling period but slows down during the 5-day forecasting period. The length of the 7-day pre-modeling period appears thus to be justified with regard to the small scale growth rate in the regional model.

OSD
4, 145–187, 2007

EGU

Comparison of the regional and GCM dynamics:

Based on Fig. 2, it has thus been shown that large scale currents are globally similar in the regional model and in the GCM. In order to give finer criteria for their comparison, the time evolution of both the regional model biases (see Eq. 11) and of the rms errors (see Eq. 12) relative to the GCM has been computed at different levels z along the 12 days of simulation (pre-modelling and forecast) and is shown in Fig. 3.

$$\text{bias}(\text{reg.}, \text{GCM}, \phi, z) = \frac{\sum_{i=1,N} \left(\phi_i^{\text{reg}}(z) - \phi_i^{\text{gcm}}(z) \right)}{N} \tag{11}$$

$$\text{rms}(\text{reg.}, \text{GCM}, \phi, z) = \sqrt{\frac{\sum_{i=1,N} \left(\phi_i^{\text{reg}}(z) - \phi_i^{\text{gcm}}(z) \right)^2}{N}} \tag{12}$$

where $\phi$is the selected variable (temperature, salinity, current) and N is the number of grid points at the depth z considered. For the GCM, we use the fields interpolated on the regional grid by VIFOP.

Such biases are thus globally small with respect to rms errors and decrease with depth. They have an opposite sign at depth of 1 m and 30 m. This leads to the conclusion that vertical gradients are smoother in the regional model than in the GCM. This is most likely due to a stronger level of turbulence in the regional model in the upper layer.

Biases being relatively small (in particular for salinity), a large part of the rms errors can be thought to be a result of small scale dynamics or of differences between meteorological forcing in regional and general circulation models. Close to the surface, large discrepancies can be observed over the salinity fields due to the differences in the river fresh water forcing strategies in both models. If explicitly forced in the regional model, such forcing is indeed applied through the relaxation of surface salinity in the GCM.

OSD
4, 145–187, 2007

Temperature, which is poorly affected by river discharges, shows a steep increase of its rms errors during the very first day. After this period of adjustment, the rms increase remains regular and smoother during the remaining of the modeling period.

3.2 Predictability at regional scale

In order to study the relevance of the 5-day forecast strategy, the forecasted fields are now compared to the hindcast reference fields. The rms errors have been computed for temperature, salinity and currents for the whole modeling period at 4 different depths over the complete domain. Figure 4 shows that rms errors remain rather small at depth. Far from the surface, these differences can most likely be associated to the differences between the forcing fields used both to initialize and force the regional model along its open boundaries: in one case the GCM forecasts are used while in the other case only analyses are considered. In the upper part of the ocean, differences in meteorological analysis – forecast forcing are mainly responsible for such mismatches which remain at a very low level probably because of the strong wind conditions which prevailed during the period.

3.3 Comparison to the observing system

The forecast issued during the 6 selected periods are now compared to satellite SST observations and to in situ MedArgo observations. A statistical analysis is given.

SST observations

The temperature at the regional model first level under the surface is compared to cloud free, AVHRR Oceans Pathfinder SST pictures which have been interpolated over the 1/16th of degree GCM grid (Marullo et al., 2006). The13-day averaged biases and the rms errors have been computed for each modeling period in order to evaluate the seasonal evolution of the errors (Fig. 5a). Biases and rms errors have been additionally

averaged over the selected forecasts in order to evaluate their evolution over a typical forecasting period (Fig. 5b).

Figure 5 clearly shows that 60 to 65% of the discrepancies between forecasts and observations are associated to a negative bias. Rms errors grow up during the first 2 to 3 days following the initialization before stabilizing. This can be due to an adjustment of the regional model initial conditions through vertical mixing. As could be expected, error levels are larger during the "stratified" periods than during the winter periods which correspond to well-mixed regimes. Indeed, in these latter cases, the influence of the turbulent scheme is much smaller.

Med-Argo observations

When and where they are available, MedArgo temperature and salinity profiles give complementary and fruitful information. They in particular offer a unique opportunity to compute both temperature and salinity biases and rms errors at depth. About 60 vertical profiles have been made by the four MedArgo profilers in the NWM region for the 6-month period (Emelianov et al., 2006). A first group of profiles is located close to the Corsica western coast while the remaining is spread in the Balearic Sea. To issue a comparison, the forecasted temperature profile at the closest grid point is selected at the observation date. Figure 6a shows for the selected periods, temperature biases and rms errors at 6 depths (8 m, 30 m, 80 m, 150 m, 300 m and 500 m).

At 8 m deep, temperature MedArgo observations lead to the same conclusion as SST satellite observations, i.e. the presence of a negative bias which is larger in fall than in winter. Even if only a few profiles are available, the differences between forecast and observations have the same order of magnitude as for SST observations. At 30 m deep, results are rather different as, when significant, the bias is positive. At 80 m deep, the differences between the regional model and the observations are rather large but are not associated to any biases.

It can thus be concluded that the underestimation of the temperature by the regional model just below the surface and its overestimation at 30 m deep can be associated

to an overestimation of the turbulent mixing. This is coherent with the conclusions of the previous section where the same regional modeling was compared to the GCM. However, at 80 m deep, the differences could rather be associated to a localized wrong representation of the water masses in fall. A similar comparison of the forecasted temperature profiles with XBT and CTD profiles (not shown) has also been carried out. It shows very similar results above 30 m, whereas at 80 m deep, the differences are much smaller than for the MedArgo observations. This would be coherent with a localized underestimation of temperature at 80 m evidenced by the MedArgo profilers.

Deeper, at 150, 300 and 500 m, Fig. 6a shows similar errors corresponding mainly to negative biases of the regional model. These errors are very close to the GCM ones (Fig. 6b) and are thus a direct consequence of the initialization. Surprisingly enough, this bias decreases during the forecast period. An explanation could be that the MedArgo observations are assimilated by the GCM and as a consequence are not independent observations. The characteristics of the different water masses and in particular of the Levantine Intermediate Waters (LIW) can thus be recovered in the GCM. Another more physical explanation could be associated to the evolution of the LIW main characteristics during the dense water formation periods in the Eastern Mediterranean basin and to their slow modification during their travel to the NWM. This study should be continued for at least one complete annual cycle to better understand the evolution of the quality of the simulations.

An analysis of the salinity errors (Fig. 6c) shows negative biases at nearly all levels. Unlike what was found for temperature, this bias does not change sign in the surface layer. It remains very close to the GCM biases (Fig. 6d). This is due to the fact that, unlike temperature, salinity does not change significantly during this short term forecast and consequently remains close to the initialization field. At depth, the salinity bias decreases with time: this was previously found for temperature.

In the surface layer, the high resolution meteorological forcing, the turbulence fluxes parameterization and the fresh water forcing are for a large part responsible for the quality of temperature and salinity vertical gradients. At depth, when the regional model

is embedded in a larger scale model and without specific assimilation, the quality of the regional scale forecast is primarily constrained by the quality of the GCM. In the NWM, the largest bias is negative affecting salinity which decreases in deeper layers but remains large in the first 100 m, leading thus to too light subsurface waters. This analysis has principally been achieved in the central region of the basin where the majority of the vertical profiles have been measured but a limited number of profiles have been additionally made directly in the Northern Current along the Spanish slope. In a further study, a distinct analysis of the bias in both water masses should provide a quantification of the errors on the horizontal density gradients and, as a consequence, on the strength and the vertical profile of the Northern Current.

4 Scale oriented analysis of several processes in the NWM

Three hydrodynamic processes have been selected, each being associated to a particular scale of the NWM dynamics. For each process, satellite images are available and are used to validate the regional model forecast. At larger scale, the general circulation and the dense water spreading are studied. At smaller scales, a wind induced coastal upwelling and the resulting vertical mixing in stratified conditions and, at coastal scales, the dispersion of the rivers fresh waters in the Gulf of Lion are then considered in details.

4.1 Main hydrologic and hydrodynamic characteristics of the Northwestern Mediterranean in winter

Observations and meteorological models show that winter 2004–2005 in the northwestern Mediterranean was characterized by periods of persistent cold and dry northerly wind. A set of deep temperature and salinity profiles sampled in the western Mediterranean during July 2005 showed that the properties of the deep water changed abruptly with a temperature drop compensating the increase accumulated in the last ten years

(Lopez-Jurado et al., 2005). These two observations suggest that strong convection took place in the MEDOC area during this winter. Both the GCM and the regional model indicate that convection broke the Levantine Intermediate Water around 42° N and 5° E at the end of January.

The satellite image of 21 January (Fig. 7a) gives information about the extent of cold waters both along the coasts and offshore. The corresponding modelling by the regional model (Fig. 7b) shows a correct localization of cold waters as well as in the Gulf of Lion as along the Spanish coasts and along the Tuscany coasts between La Spezia and Livorno.

Offshore, cold waters are isolated from the coast by the Northern Current perceptible by its higher temperature from the Corsica channel till the western tip of the Gulf of Lion. At this point, the simulation results indicate that the current is divided into two veins: one is characterized by less intense currents sticks to the Spanish slope bounding the shelf narrow in the north and widening near the Ebro mouth while the other turns southward and follows a cyclonic pathway around the convection area. Between the Balearic Islands, the warmer and less saltier Atlantic water flowing from the south of the basin penetrates northward beyond 41° N which does not look realistic compared to the satellite image.

The simulations indicate that the weakening of the alongslope vein of the northern current and the corresponding strengthening of the south branch of the cyclonic circulation is likely linked to strong wind bursts in the Gulf of Lion. However observations of slope currents in the region do not seem to corroborate this process (Jordà, 2005). The underestimation by models of salinity (Sect. 3.3) and density in the subsurface waters could be responsible of erroneous circulation patterns in this region.

4.2 Wind induced coastal upwelling and mixing in stratified conditions: the case of 25 September 2004

The period of the 20 to the 24 of September is characterized by a north-western wind blowing over the Gulf of Lion and extending over the western Ligurian Sea (Fig. 8a).

Then, starting on the 25th, a classical configuration of winds settles over the region of the Gulf of Lion. It is made of the canalized Mistral and Tramontane winds (Fig. 8b). In both situations, the northern part of the Gulf of Lion is in upwelling conditions. This can clearly be seen both on the satellite picture (Fig. 9a) and on the regional forecast (Fig. 9b) where cold waters appear along the coast. The coastal region is not the only area where waters have been cooled down, as the strong wind burst has strongly cooled offshore waters.

The Gulf of Genoa and the region of the Corsica Island are isolated from the wind burst and consequently appear warmer both on satellite picture and in the regional forecast. Southwest of the Gulf of Lion, only the Ebro valley is submitted to a significant wind forcing. Over this region, this wind has yet for consequence a slight cooling of the sea surface while the surrounding waters remain warmer. Such warmer waters can also be found along the coast south of the Ebro mouth. The largest mismatch of the model forecast can be found north of the Majorca Island with much colder waters than in the satellite picture.

These winds have a strong influence on the Northern current at the eastern entrance of the Gulf of Lion. The influence of the northern winds on the Northern Current is yet poorly known. Estournel and al. (2003) have shown that, in Mistral and Tramontane conditions, a branch of the Northern current could penetrate over the western part of the shelf (around longitude 3.5° E). Satellite picture and model results allow to study the consequence on the current of the wind regime change occurring on September 25. During the first wind period of Fig. 8a, the surface current characterized by relatively warm waters seems to be stopped along the Ligurian coast at about 6° E of longitude (Fig. 9a). A steep thermal front separates these waters from the colder upwelling waters which are spreading from the north-eastern coast of the Gulf of Lion. During the Mistral and Tramontane period of Fig. 8b, the eastern part of the Gulf is not submitted to strong wind conditions and a positive wind curl settles down east of the Rhone valley. On 28 September, the SST satellite image (Fig. 9c) shows that the Northern current has progressed along the coast in the direction of the Rhone river mouth. The 1.5 km

high-resolution coastal forecast issued with the embedded coastal model is analyzed to further study this process. Figure 10 shows a superimposition of the forecasted surface temperatures and currents for the 25 and the 29 of September. At the eastern boundary of the Fig. 10a, the Northern current separates into a coastal branch which is blocked by the upwelling colder waters and a second offshore branch. On Fig. 10b, the coastal branch of the current has progressed further and clearly penetrates over the shelf between Marseille and the Rhone river mouth.

No clear dynamical mechanism has so far been proposed to explain this process: either the decrease of the wind strength in the eastern part of the shelf or the wind curl could for instance offer local explanations for the current behavior. Otherwise, a consequence of the Tramontane wind is to push the water outside the Gulf of Lion shelf in its south-western part (Estournel et al., 2003 ; Ulses et al., 2006). This process could also have a remote influence on the incoming of the Northern current over the eastern part of the Gulf. The understanding and the quality of the representation by the models of these shelf/slope exchanges is crucial as it governs the renewal of the shelf waters.

4.3 Dispersion of freshwater in the Gulf of Lion in winter

The Rhone River carries 90% of the fresh water discharge over the Gulf of Lion and the remaining 10% comes from several smaller rivers located west of the Rhone river mouth. Surface temperatures observed by satellite do not allow for a clear distinction between fresh and salty waters. When conditions are favourable, fresh waters originating from the rivers can however be distinguished using satellite images of the water colour, such as observations of chlorophyll or of the suspended matter concentrations although the relation with salinity is obviously not direct. The satellite SST and the A-chlorophyll surface concentration on 1 January 2005 are given respectively on Figs. 11a and b.

On these pictures, the correlations between cold waters and waters rich in A-chlorophyll are rather large and, on the northern part of the Gulf, a large, overspread pattern of cold and rich waters can be observed between longitudes ranging between

4° E and 5° E. Such waters are most likely originating from the Rhone River. On the western part of the Gulf, waters with similar characteristics can also be found in the near shore area but we cannot conclude that they originate from river discharges. Indeed, in this area, the fresh water discharges are rather small and the river mouths are spread along the coastline preventing the identification of individual plumes.

Figures 12a and b show the surface temperature and salinity as forecasted by the high resolution coastal model of the Gulf of Lion. Cold and fresh waters can also be found in the near-shore area. On the northern part, the Rhone River plume is well represented in particular between 4.5° and 5° E. The North South oriented distal part of the plume (located at 4.15° E) corresponding to more diluted waters is, in the coastal forecast, located west of their observed position and show a more west-east orientation. Along the western coast of the Gulf, cold and fresh waters can also be found.

The outer shelf exhibits warmer waters originating from the shelf break. The forecast shows indeed that these waters progress across the slope through several canyons, which can explain the chaotic shape of the front separating the shelf break warm waters from the cold waters found over the shelf.

As far as the meteorological situation is concerned, strong north to north-west winds have been blowing for 16 days over the Gulf of Lion, the strongest winds being found in the south-western area. The presence of cold waters along the coastline can thus be explained both by the strength and the duration of this cold wind event. The forecast clearly indicates that, along the western coast, the effect of temperature to increase density is larger than the opposite one of salinity, leading to waters which are denser than mid-shelf waters contrary to what happens in the Rhone mouth area. This is due to the rather low river discharges in the western part of the Gulf. The intrusions of slope water onto the shelf are associated to shelf break upwelling forced by northwest winds.

As a conclusion, dense coastal waters are present on the inner shelf next to lighter offshore waters on the outer shelf. The motion of these two water masses is principally forced by winds. Indeed, wind bursts have a crucial impact to upwell slope waters

and to densify near-shore waters and advect them toward the south-west following the isobaths. It seems clear from the forecast modeling and satellite observations, that coastal waters are flushed from the Gulf of Lion toward the South-West in the area of Cap Creus. The simulation indicates that dense waters enter the Cap Creus canyon and follow the western part of the canyon under the effect of the Coriolis acceleration. An upwelling is located over the opposite (eastern) side of the canyon. Such dynamical processes are associated to small scale bathymetric features and, as a consequence, can only be forecasted in high resolution model, which confirms (if needed) the necessity of the two-step (basin scale to regional and regional to coastal) embedded modeling of the NWM.

5 Concluding remarks

In the frame of the Mediterranean Forecasting System, we have developed an embedded forecasting system in the North Western Mediterranean including a 3 km×3 km regional model and a 1.5 km×1.5 km coastal model. This project gave us the opportunity to move from classical "process oriented studies" to more realistic "scale oriented studies" and to achieve long term forecast of the NWM in which processes are validated at each stage of the embedded modeling. In the present configuration, dedicated observations have been assimilated in the basin scale GCM.

The coastal and regional NWM embedded forecasting system is based on the Symphonie hydrodynamic free surface model and on the variational initialization and forcing platform VIFOP. A 5-day forecast can be issued after a pre-modeling period of 7 days. This is one of the main results of the present study. Indeed, it has been shown that the development of small scale processes necessitates a one week "hindcast" (pre-modeling period) during which the forecasting capability of the embedded model is dubious. This was confirmed by a comparison of the evolution of the small scale kinetic energy in the low and high resolution models.

The embedded NWM forecasts have been compared to the MFS observing sys-

tem. It was basically found that in the first 100 m under the surface, the NWM model forecasts are characterized by large negative biases of salinity leading thus to too light subsurface waters. These biases are very close to the GCM ones as salinity is strongly dependent of the initial conditions for such short runs. Deeper at 150, 300 and 500 m, the negative bias is reduced and above all, it decreases gradually as time goes along. It will be interesting to understand if the assimilation of ARGO profiles is responsible of these improvements. Concerning temperature, its underestimation by the regional model just below the surface and its overestimation at 30 m deep can be associated to an overestimation of the turbulent mixing.

To conclude this scale oriented study of the NWM dynamics, we focused on processes at three characteristic scales: the regional distribution of dense water in winter, a wind induced upwelling and, at smaller scale, the spreading of freshwater on the shelf area.

The regional and coastal models allow to represent a number of processes especially those induced by the wind as coastal upwelling under stratified conditions, dense water formation over the Gulf of Lion shelf, deep mixing in the convection zone or influence on the Northern Current penetration in the Gulf of Lion. On the other hand, some doubtful regional features as the circulation in the Catalan Sea should be studied in more detail especially by taking a careful look to available observations. The increasing volume of data available thanks to MFS should allow us to better understand the major drawbacks of the modeling system and then to contribute to improve it at its different scales.

Appendix A

Model equations in sigma coordinate system

Momentum equations under Boussinesq approximation are given by:

$$\frac{\partial \tilde{u}}{\partial t^*} + \frac{\partial \tilde{u}u}{\partial x^*} + \frac{\partial \tilde{v}u}{\partial y^*} + \delta\sigma\frac{\partial \omega u}{\partial \sigma} - f\,\tilde{v} = \frac{-D}{\rho_0}\frac{\partial p}{\partial x} + \frac{\partial}{\partial x^*}\tilde{K}^x\frac{\partial u}{\partial x^*} + \frac{\partial}{\partial y^*}\tilde{K}^y\frac{\partial u}{\partial y^*} + \frac{\delta\sigma}{h+\eta}\frac{\partial}{\partial\sigma}K^z\frac{\partial u}{\partial\sigma} \quad \text{(A1)}$$

$$\frac{\partial \tilde{v}}{\partial t^*} + \frac{\partial \tilde{u}v}{\partial x^*} + \frac{\partial \tilde{v}v}{\partial y^*} + \delta\sigma\frac{\partial \omega v}{\partial \sigma} + f\,\tilde{u} = \frac{-D}{\rho_0}\frac{\partial p}{\partial y} + \frac{\partial}{\partial x^*}\tilde{K}^x\frac{\partial v}{\partial x^*} + \frac{\partial}{\partial y^*}\tilde{K}^y\frac{\partial v}{\partial y^*} + \frac{\delta\sigma}{h+\eta}\frac{\partial}{\partial\sigma}K^z\frac{\partial v}{\partial\sigma} \quad \text{(A2)}$$

The stars indicate that the variables are in the sigma coordinate system and the tilde variables refer to a multiplication by the corresponding layer thickness D given by $D=(h+\eta)\delta\sigma$ (e.g.: $\tilde{u}=Du$) where h is the motionless water depth, η the surface elevation anomaly and $\delta\sigma$ the sigma increment. The hydrostatic approximation in sigma coordinates, leads to the following formulation of the horizontal pressure gradient:

$$-\frac{1}{\rho_0}\frac{\partial p}{\partial x} = -g\frac{\partial \eta}{\partial x} - \frac{1}{\rho_0}\left(\frac{\partial p'}{\partial x^*} + \frac{\partial z}{\partial x^*}g\rho'\right) \quad \text{(A3)}$$

where $p'=g\int_z^\eta \rho' dz'$ is the hydrostatic pressure associated to the density anomaly :$\rho'=\rho-\rho_0$.

Density is related to temperature and salinity via the state equation, and the evolution of temperature and salinity is given by:

$$\frac{\partial \tilde{T}}{\partial t^*} + \frac{\partial \tilde{u}T}{\partial x^*} + \frac{\partial \tilde{v}T}{\partial y^*} + \delta\sigma\frac{\partial \omega T}{\partial \sigma} = \frac{\partial}{\partial x^*}\tilde{K}^x\frac{\partial T}{\partial x^*} + \frac{\partial}{\partial y^*}\tilde{K}^y\frac{\partial T}{\partial y^*} + \frac{\delta\sigma}{h+\eta}\frac{\partial}{\partial\sigma}K^z\frac{\partial T}{\partial\sigma} + \frac{\delta\sigma}{\rho C_p}\frac{\partial Q}{\partial\sigma} \quad \text{(A4)}$$

$$\frac{\partial \tilde{S}}{\partial t^*} + \frac{\partial \tilde{u} S}{\partial x^*} + \frac{\partial \tilde{v} S}{\partial y^*} + \delta\sigma \frac{\partial \omega S}{\partial \sigma} = \frac{\partial}{\partial x^*} \tilde{K}^x \frac{\partial S}{\partial x^*} + \frac{\partial}{\partial y^*} \tilde{K}^y \frac{\partial S}{\partial y^*} + \frac{\delta\sigma}{h+\eta} \frac{\partial}{\partial \sigma} K^z \frac{\partial S}{\partial \sigma} \quad \text{(A5)}$$

where $\frac{\partial Q}{\partial z}$ is the solar radiative heat flux forcing. This flux is related to its surface value through a double exponential decrease as stated by Paulson and Simpson (1977):

$$\frac{Q}{Q_S} = 0.42\, e^{\frac{z}{23}} + 0.58\, e^{\frac{z}{0.35}} \quad \text{(A6)}$$

The continuity equation is given by:

$$\frac{\partial \tilde{u}}{\partial x^*} + \frac{\partial \tilde{v}}{\partial y^*} + \delta\sigma \left(\frac{\partial \omega}{\partial \sigma} + \frac{\partial \eta}{\partial t^*} \right) = 0 \quad \text{(A7)}$$

In the generalized sigma coordinate system, $\delta\sigma$ is likely to be a function of the horizontal coordinates x and y whereas in the usual "simple" sigma coordinate system $\delta\sigma$ is a constant of x and y but can depend on the vertical coordinate leading to a higher vertical resolution near the bottom or the surface. In this latter case, the above equations are similar to the classical sigma coordinate equations. When $\delta\sigma$ is independent of the horizontal coordinate, the continuity equation (A7) leads for instance to:

$$\frac{\partial (h+\eta) u}{\partial x^*} + \frac{\partial (h+\eta) v}{\partial y^*} + \frac{\partial \omega}{\partial \sigma} + \frac{\partial \eta}{\partial t^*} = 0 \quad \text{(A8)}$$

References

Adcroft, A., Hill, C., and Marshall, J.: Representation of Topography by Shaved Cells in a Height Coordinate Ocean Model, Monthly Weather Rev., 125, 9, 2293–2315, 1997.

Auclair, F., Marsaleix, P., and Estournel, C.: Sigma coordinate pressure gradient errors : evaluation and reduction by an inverse method, J. Atmos. Oceanic Technol., 17, 1348–1367, 2000a.

Auclair, F., Casitas, S., and Marsaleix, P.: Application of an inverse method to coastal modelling, J. Atmos. Oceanic Technol., 17, 1368–1391, 2000b.
Auclair, F., Marsaleix, P., and Estournel, C.: The penetration of the northern current over the Gulf of Lion (western Mediterranean Sea) as a downscaling problem, Oceanologica Acta, 24, 529–544, 2001.
Auclair, F., Estournel, C., Marsaleix, P., and Pairaud, I.: On coastal ocean embedded modelling, Geophys. Res. Lett., 33, L14602, doi:10.1029/2006GL026099, 2006.
Blumberg, A. F. and Mellor, G. L.: A description of a three-dimensional coastal circulation model, Three-Dimensional Coastal Ocean Models, Coastal Estuarine Sci., vol. 4, Ed. N. Heaps, AGU, Washington, D.C., 1–16, 1987.
Brozkova, R., Derkova, M., Bellus, M., and Farda, A.: Atmospheric forcing by ALADIN/MFSTEP and MFSTEP oriented tunings, Ocean Sci., 2, 113–121, 2006, http://www.ocean-sci.net/2/113/2006/.
Demirov, E. and Pinardi, N.: The Simulation of the Mediterranean Sea circulation from 1979 to 1993. Part I: The interannual variability, J. Mar. Syst., 33–34, 23–50, 2002.
Dufau-Julliand, C., Marsaleix, P., Petrenko, A., and Dekeyser, I.,: Three-dimensional modeling of the Gulf of Lion's hydrodynamics (northwest Mediterranean) during Jannuary 1999 (MOOGLI3 Experiment) and late winter 1999: Western Mediterranean Intermediate Water's (WIW's) formation and its cascading over the shelf break, J. Geophys. Res., 109, C11002, doi:10.1029/2003JC002019, 2004.
Emelianov, M., Font, J., Turiel, A., Solé, J., Poulain, P., Julià, A., and Vitrià, M. R. : Transformation of Levantine Intermediate Water tracked by MedArgo floats in Western Mediterranean, Ocean Sci., 2, 281–290, 2006, http://www.ocean-sci.net/2/281/2006/.
Estournel, C., Kondrachoff, V., Marsaleix, P., and Vehil, R.: The plume of the Rhône : numerical simulation and remote sensing, Continental Shelf Res., 17, 899–924, 1997.
Estournel, C., Broche, P., Marsaleix, P., Devenon, J. L., Auclair, F., and Vehil, R.: The Rhone river plume in unsteady conditions : numerical and experimental results. Estuarine, Coastal and Shelf Sci., 53, 25–38, 2001.
Estournel, C., Durrieu de Madron, X., Marsaleix, P., Auclair, F., Julliand, C., and Vehil, R.: Observation and modelisation of the winter coastal oceanic circulation in the Gulf of Lions under wind conditions influenced by the continental orography (FETCH experiment), J. Geophys. Res., 108(C3), 7-1–7-18, 2003.

Gaspar, P., Grégoris, Y., and Lefevre, J. M.: A simple eddy kinetic energy model for simulations of the oceanic vertical mixing : tests at station Papa and long-term upper ocean study site, J. Geophys. Res., 95, 179–193, 1990.
Geernaert, G. L.: Bulk parameterizations for the wind stress and heat fluxes, in: Surface waves and fluxes, Vol I, edited by: Geernaert, G. L. and Plant, W. J., 91–192, 1999.
Guizien, K., Brochier, T., Duchêne, J.-C., Koh, B.-S., and Marsaleix, P.: Dispersal of owenia fusiformis larvae by wind-driven currents: turbulence, swimming behaviour and mortality in a three-dimensional stochastic model, Mar. Ecol. Prog. Ser., 311, 47–66, 2006.
Haney, R. L.:. On the Pressure Gradient Force over Steep Topography in Sigma Coordinate Ocean Models, J. Phys. Oceanogr., 21, 610–619, 1991.
Johns, B., Marsaleix, P., Estournel, C., and Vehil, R.: On the wind-driven upwelling circulation in the Gulf of Lions, J. Mar. Syst., 3, 309–320, 1992.
Jorda Sanchez, G.: Towards data assimilation in the Catalan continental shelf – From data analysis to optimization methods. Ph.D. Thesis University of Barcelona, 2005.
Lopez-Jurado, J.-L., Gonzalez-Pola, C., and Velez-Belchi, P.: Observation of an abrupt disruption of the long-term warming trend at the Balearic Sea, western Mediterranean Sea, in summer 2005, Geophys. Res. Lett., 32, L24606, doi:10.1029/2005GL024430, 2005.
Marsaleix, P., Estournel, C., Kondrachoff, V., and Vehil, R.: A numerical study of the formation of the Rhone river plume, J. Mar. Syst., 14, 99–115, 1998.
Marsaleix, P., Auclair, F., and Estournel, C.: Considerations on open boundary conditions for regional and coastal ocean models, J. Atmos. Oceanic Technol., 23, 1604–1613, 2006.
Marullo, S., Buongiorno Nardelli, B., Guarracino, M., and Santoleri, R.: Observing the Mediterranean Sea from space: 21 years of Pathfinder-AVHRR Sea Surface Temperatures (1985 to 2005), Re-analysis and validation, Ocean Sci. Discuss., 3, 1191–1223, 2006, http://www.ocean-sci-discuss.net/3/1191/2006/.
Millot, C.: The Gulf of Lions' hydrodynamics, Cont. Shelf Res., 10(9–11), 885–894, 1990.
Paulson, C. A. and Simpson, J. J.: Irradiance Measurements in the upper ocean, J. Phys. Oceanogr., 7, 952–956, 1977.
Petrenko, A., Leredde, Y., and Marsaleix, P.: Circulation in a stratified and wind-forced Gulf of Lions, NW Mediterranean Sea : in-situ and modeling data, Cont. Shelf Res., 25, 7–27, 2005.
Pietrzak, J., Jakobson, J. B., Burchard, H., Vested, H. J., and Petersen, O.: A three-dimensional hydrostatic model for coastal and ocean modelling using a generalised topography following co-ordinate system, Ocean Modelling, 4, 173–205, 2002.

Pinardi, N., Auclair, F., Cesarini, C., Demirov, E., Fonda-Umani, S., Giani, M., Montanari, G., Oddo, P., Tonani, M., and Zavatarelli, M.: Toward marine environmental prediction in the Mediterranean Sea coastal areas: a monitoring approach. In Ocean Forecasting : conceptual basis and applications, edited by: Pinardi, N., Springer Verlag, 2001.

Reffray, G., Fraunié, P., and Marsaleix, P.: Secondary flows induced by wind forcing in the Rhône region of freshwater influence, Ocean Dyn. 54, 179–196, 2004.

Ulses, C., Grenz, C., Marsaleix, P., Schaaff, E., Estournel, C., Meulé, S., and Pinazo, C.: Circulation in a semi enclosed bay under the influence of strong fresh water input, J. Mar. Syst., 56, 113–132, 2005.

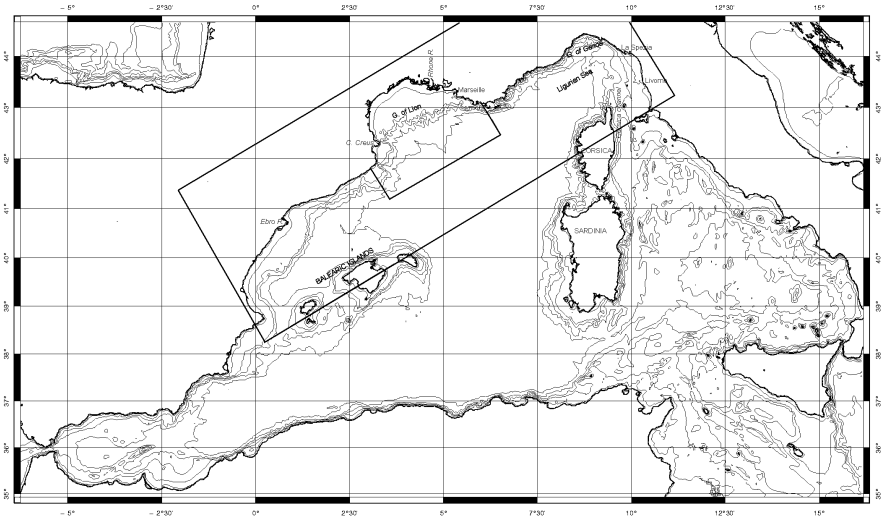

Fig. 1. Implementation of the Northwestern Mediterranean regional model and of the Gulf of Lion coastal model.

OSD

4, 145–187, 2007

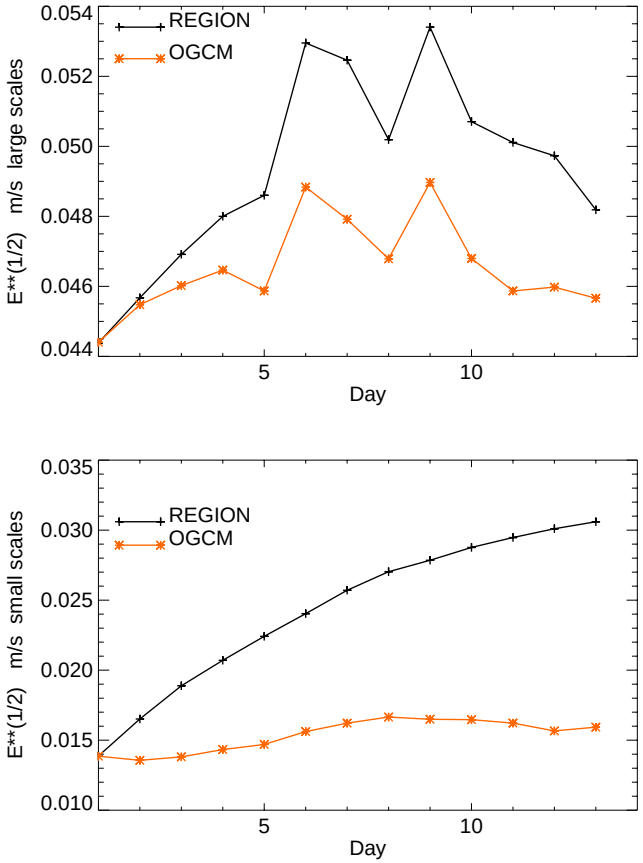

Fig. 2. Mean evolution of the spatially averaged kinetic energy root mean square during the twelve days of simulation. Kinetic energy has been splitted in a large scale component and small scale component. Results are presented for the regional model and for the OGCM.

OSD
4, 145–187, 2007

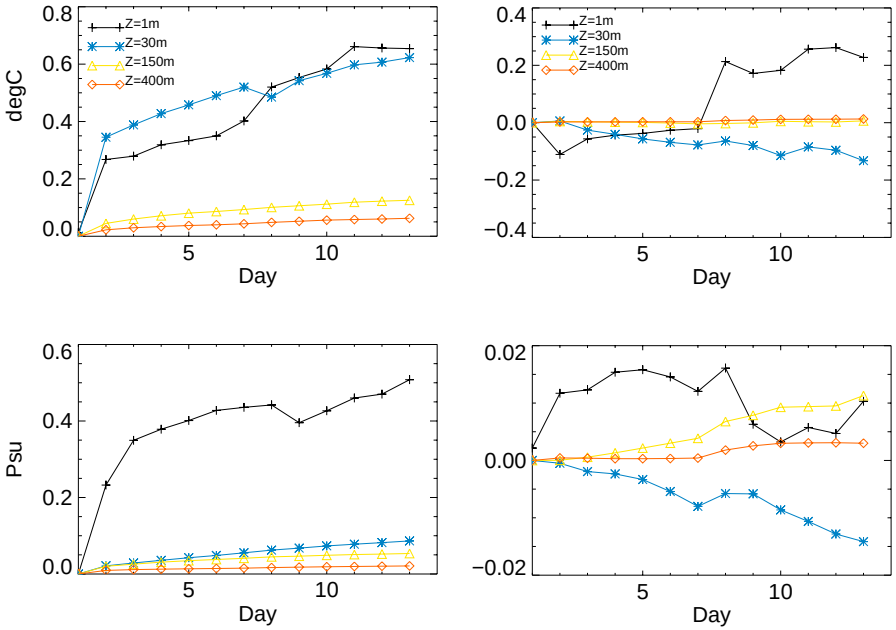

Fig. 3. Bias (right panel) and rms error (left panel) of the regional model with respect to OGCM calculated for temperature (upper panel) and salinity (lower panel) at different levels.

OSD
4, 145–187, 2007

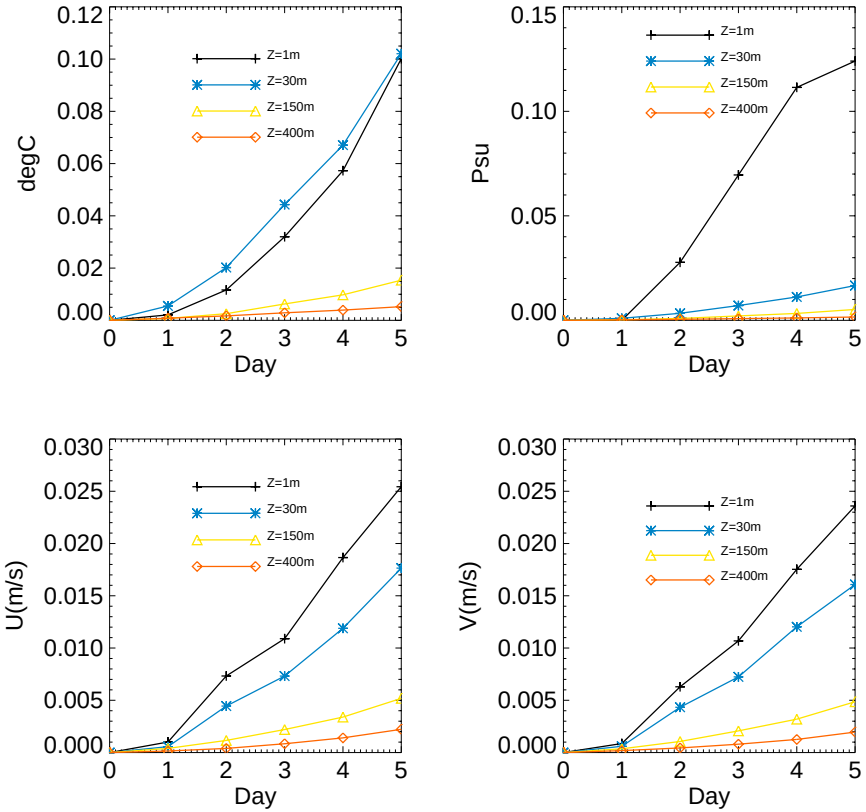

Fig. 4. Evolution of the rms error of the forecast with respect to the hindcast calculated for temperature, salinity and the two components of the current at different levels.

OSD
4, 145–187, 2007

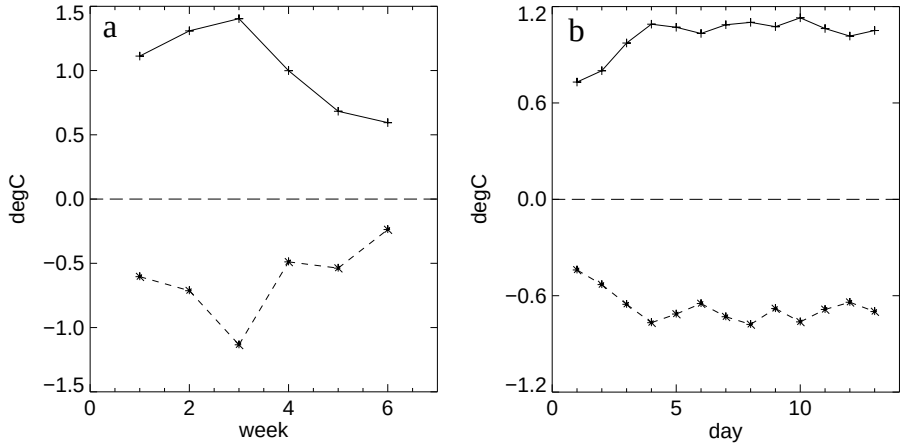

Fig. 5. rms error (upper panel) and bias (lower panel) of the regional model with respect to satellite SST. **(a)**: Each point corresponds to an average over a 13-day forecasting period; **(b)**: Each point corresponds to a daily average of the six selected forecast periods.

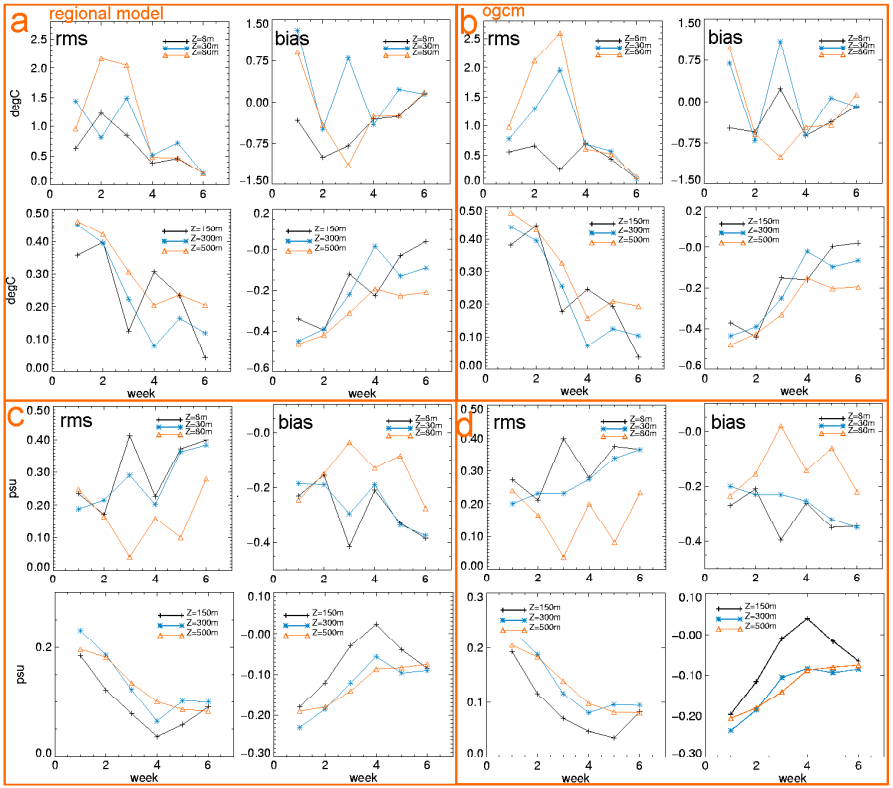

Fig. 6. **(a)** and **(c)** : rms error and bias of the regional model with respect to MedArgo temperature and salinity observations. **(b)** and **(d)** rms error and bias of the MFSTEP OGCM with respect to MedArgo temperature and salinity observations on the domain of the NWM model.

OSD
4, 145–187, 2007

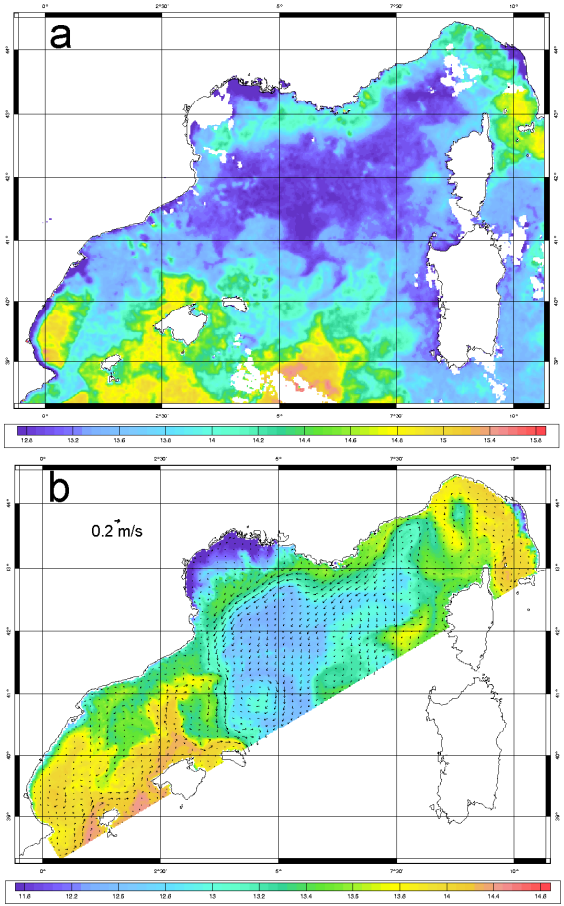

Fig. 7. Sea surface temperature **(a)** from NOAA AVHRR satellites distributed by DLR **(b)** from the NWM regional model corresponding to the 21 January 2005. The simulated current at 20 m under the surface has been superimposed on (b).

OSD
4, 145–187, 2007

EGU

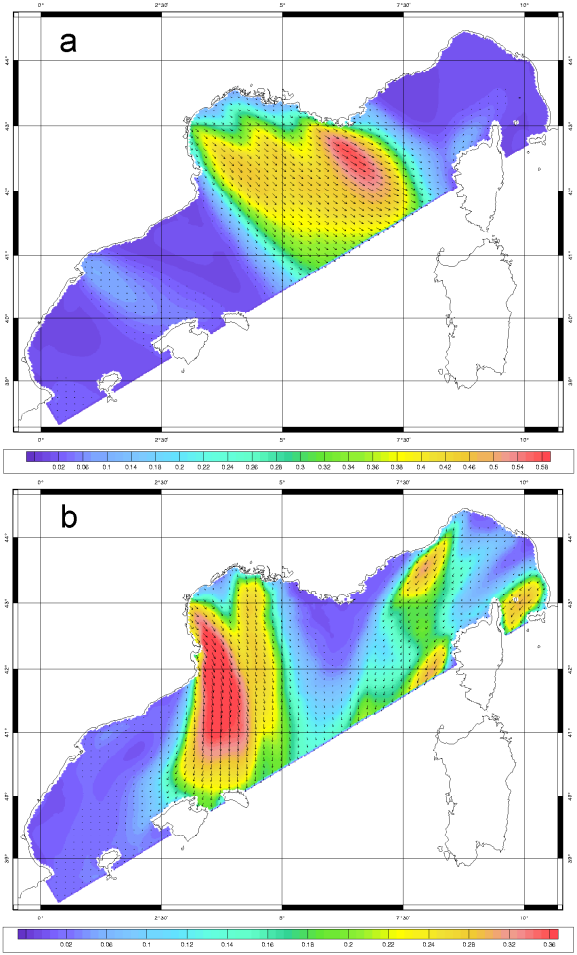

Fig. 8. Wind stress (N/m2) calculated from the ALADIN model wind for **(a)** 24 September 2004 **(b)** 27 September 2005.

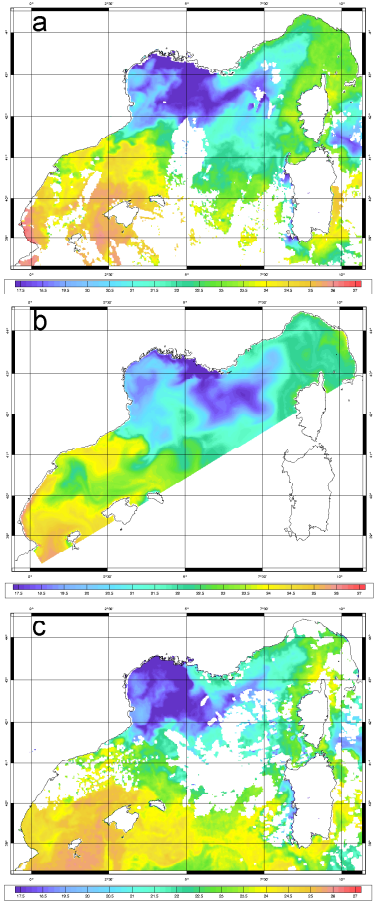

Fig. 9. Sea surface temperature **(a)** from NOAA AVHRR satellites distributed by DLR for 25 September 2004 **(b)** from the NWM regional model for 25 September 2004 **(c)** from NOAA AVHRR satellite for 28 September 2004.

OSD
4, 145–187, 2007

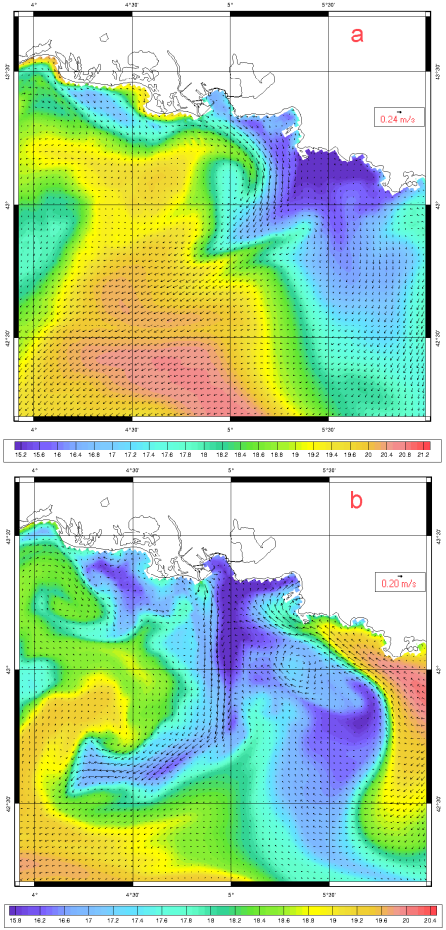

Fig. 10. Surface current superimposed on sea surface temperature simulated by the Gulf of Lion model for **(a)** 25 September 2004 **(b)** 29 September 2004.

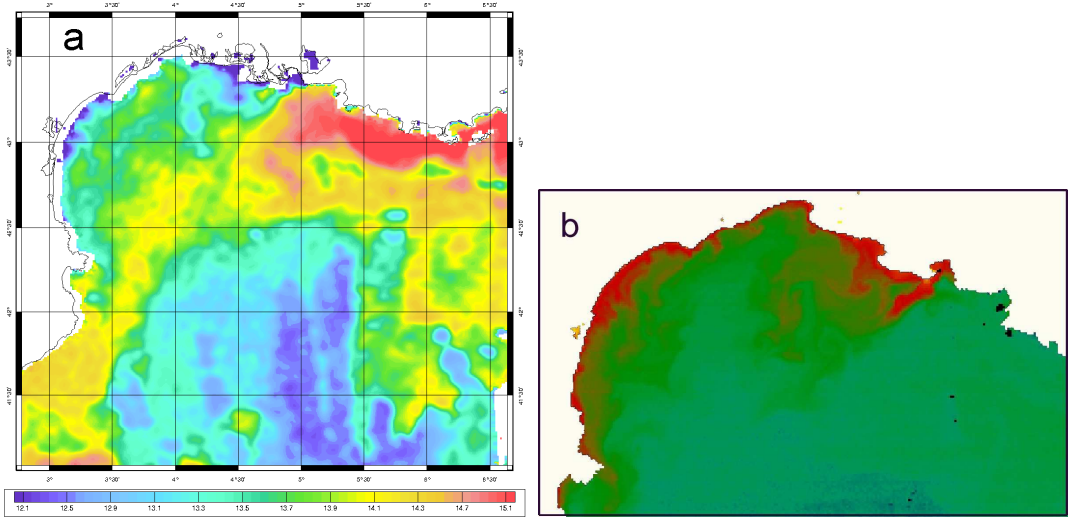

Fig. 11. **(a)** Sea surface temperature from NOAA AVHRR satellites distributed by DLR for 1 January 2005. **(b)** Map of A-chlorophyll surface concentration from MODIS (distributed by NASA).

OSD
4, 145–187, 2007

EGU

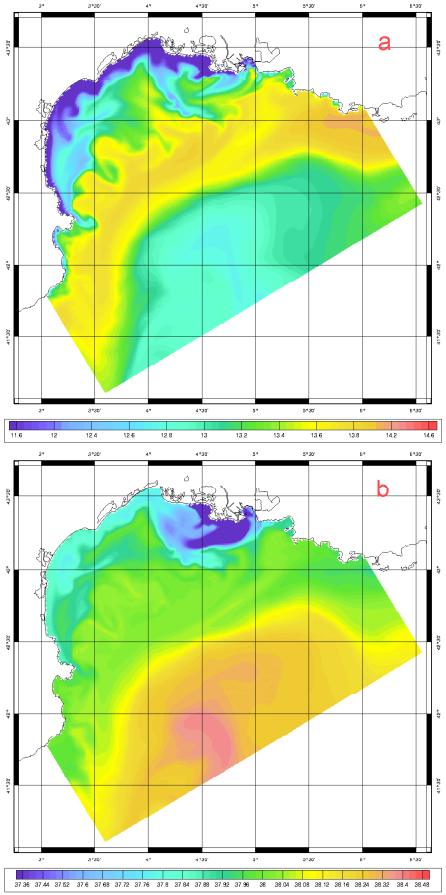

Fig. 12. Sea surface temperature **(a)** and sea surface salinity **(b)** simulated by the Gulf of Lion model for 1 January 2005.

OSD
4, 145–187, 2007

EGU